

Research paper

Topological shape optimization of 3D micro-structured materials using energy-based homogenization method

Gao Jie, Li Hao, Gao Liang, Xiao Mi*

State Key Lab of Digital Manufacturing Equipment and Technology, Huazhong University of Science and Technology, 1037 Luoyu Road, Wuhan, Hubei 430074, China



ARTICLE INFO

Keywords:

Micro-structured materials
Topology optimization
Energy-based homogenization method
Parametric level set method
Periodic boundary formulation

ABSTRACT

This paper proposes an effective method for the design of 3D micro-structured materials to attain extreme mechanical properties, which integrates the firstly developed 3D energy-based homogenization method (EBHM) with the parametric level set method (PLSM). In the 3D EBHM, a reasonable classification of nodes in periodic material microstructures is introduced to develop the 3D periodic boundary formulation consisting of 3D periodic boundary conditions, 3D boundary constraint equations and the reduced linearly elastic equilibrium equation. Then, the effective elasticity properties of material microstructures are evaluated by the average stress and strain theorems rather than the asymptotic theory. Meanwhile, the PLSM is applied to optimize micro-structural shape and topology because of its positive characteristics, like the perfect demonstration of geometrical features and high optimization efficiency. Numerical examples are provided to demonstrate the advantages of the proposed design method. Results indicate that the optimized 3D material microstructures with expected effective properties are featured with smooth structural boundaries and clear interfaces.

1. Introduction

Micro-structured materials consist of a number of periodically arranged microstructures and possess some superior performance, such as the higher specific stiffness and strength, better fatigue strength and improved corrosion-resistance [1,2]. Currently, this kind of materials has gained extensive applications in various engineering fields. For example, the typical cellular honeycomb composites composed of an array of periodic unit cells (PUCs) have been employed in automobile and aerospace industries [3]. Although PUCs are fashioned with regular constituent materials, like metal and foam, many superior and extraordinary properties mentioned-above at the bulk scale can be presented. The main reason is that the macroscopic performance of cellular composites mainly depends on the configurations of PUCs rather than the constituent compositions [4,5]. Up to now, an increasing number of publications have reported on the modification of the geometrical sizes and shapes of microstructures to enhance their properties. However, these related existing methods are recognized to be experimental or intuitive [6].

Computational topology optimization has long been recognized as a powerful tool for the optimization of both structures and materials, which offers a systematic and scientific driven framework for design [7–10]. The basic idea is that materials are iteratively eliminated and redistributed within a given design domain to seek the best material

distribution with the optimal performance under some prescribed constraints. This research field has undergone remarkable developments in recent years and various topology optimization methods have been developed, such as the homogenization method [11], solid isotropic material with penalization (SIMP) method [12,13], evolutionary structural optimization (ESO) method [14], and level set method (LSM) [15–17]. Meanwhile, since the homogenization theory [18] is developed to evaluate macroscopic effective properties based on the topologies of periodical material microstructures, it has become popular to combine the homogenization theory with topology optimization to formulate an inverse design procedure of PUCs for gaining the specific effective properties [19]. Many researchers have devoted considerable efforts to optimize or tailor material effective properties, so that micro-structured materials with various novel effective properties have been presented, such as the extreme mechanical properties [20–23], maximum stiffness and fluid permeability [24,25], exotic thermo-mechanical properties [26], negative Poisson's ratio (NPR) [27–30] and extreme thermal properties [31]. Micro-structured materials design has become one of the most promising applications of topology optimization [7,32].

In majority of the existing works for the optimization of PUCs, numerical homogenization method (NHM) works as the bridge between the design of materials and topology optimization to evaluate material effective properties. It is well-known that the asymptotic expansion

* Corresponding author.

E-mail address: xiaomi@hust.edu.cn (M. Xiao).

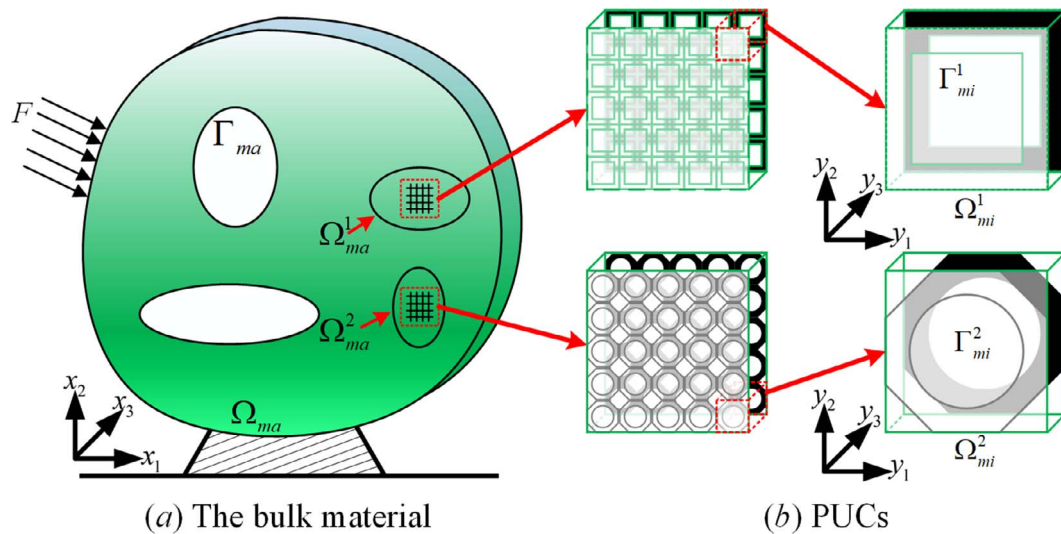


Fig. 1. The bulk material composed of two kinds of PUCs.

theory is the basic framework of the NHM, while its theoretical derivations and numerical implementations are complex [33,34]. For example, a fictitious body force is formulated under the imposing of the initial unit test strains on PUCs to solve the induced strain field in the finite element analysis [35]. Moreover, the NHM would be hard to be directly connected with topology optimization for materials design [28]. Hence, as an alternative way, the energy-based homogenization method (EBHM) with simple theoretical analysis and easy numerical implementations is proposed [28]. The key idea is that the average stress and strain theorems act as the theoretical basis to evaluate effective properties by reasonably imposing the initial unit test strains to construct the periodic boundary formulation. Until now, the EBHM gains great applications, such as combining with hybrid cellular automata [30], lattice structures [36], advanced structures and materials [37,38]. However, only the 2D periodic boundary formulation in the EBHM is developed to design 2D micro-structured materials with extreme effective properties. In the view of real-world engineering design problems, the design of 3D micro-structured materials is much more common and meaningful.

On the other side, the LSM is applied to optimize structures by evolving structural boundaries rather than material layouts in material distribution model, so that the optimized structures have smooth boundaries and are free of grayscale. Since the seminar work of Sethian and Wiegmann [15], the LSM has been quickly expanded to solve a broad range of optimization problems [39–41], including materials design [42,43]. However, due to directly solving the H-J PDE, some unfavorable numerical implementations with strict requirements are involved in the standard LSM [16,17] (e.g. Courant-Friedrichs-Lewy (CFL) condition, re-initialization and boundary velocity extension), which may hinder its further applications. In response to the numerical issues, many variants of the LSM are proposed [44–48]. One of them, termed as the parametric LSM (PLSM) [49,50], would be a powerful alternative LSM for handling topological shape optimization problems due to that the intrinsic desired features (e.g. the perfect demonstration of structural features) are kept while avoiding the difficulties of the LSM. The central idea is the interpolation of the level set function by a given set of the compactly supported radial basis functions (CSRBFs). Thus, the initial complicated PDE-driven shape topology optimization problem can be converted into a much easier “size” optimization problem. Moreover, many well-established optimization algorithms can be directly applied to evolve design variables, e.g. the optimality criteria (OC) method [12] and the method of moving asymptotes (MMA) [51]. Many optimization problems have been successfully solved by the PLSM, like the compliant mechanism [52], manufacturing constraints

[53], robust optimization [54], multi-materials [55], and functional graded cellular composites [56].

In the present work, an effective design method for 3D micro-structured materials is proposed, where the 3D EBHM is developed to evaluate material effective properties and the PLSM is applied to evolve structural topologies. In the 3D EBHM, the 3D periodic boundary formulation is elaborated from three key factors: the imposing of the 3D periodic boundary conditions, the development of the 3D boundary constraint equations and the derivation of the reduced linearly elastic equilibrium equation. Firstly, the initial unit test strains are only imposed on the structural boundaries including the vertices, edges and surfaces of 3D microstructures to maintain the periodicity and continuity conditions in the bulk material. Then, a reasonable classification of nodes in a 3D PUC is defined to develop the boundary constraint equations, so that the periodic boundary conditions are illustrated in an explicit way to directly impose on the boundaries of PUCs. Finally, a direct solution scheme is employed to derive the reduced linearly elastic equilibrium equation for solving the displacement field in the finite element analysis. Due to the use of the PLSM, the optimized structures are free of the grayscale and zigzag interfaces, which are problematic in the engineering sense because the obtained optimal solutions are difficult to be interpreted as the manufacturable designs.

The remainder of this paper is organized as follows. A brief introduction about the homogenization theory is given in Section 2. Section 3 provides a detailed description of the 3D EBHM, including periodic boundary conditions, boundary constraint equations and the reduced linearly elastic equilibrium equation. In Section 4, the mathematical model of 3D micro-structured materials design is provided. Section 5 presents the detailed numerical implementations. Numerical examples are provided to illustrate the advantages of the proposed method in Section 6. Conclusions and further work are displayed in Section 7.

2. Homogenization theory

The homogenization theory is applied to evaluate material effective properties by directly analyzing the periodically distributed material unit cells, i.e., material microstructures. It includes two assumptions: (1) the dimensional sizes of PUCs are much smaller than that of the bulk material; and (2) PUCs are periodically distributed in the bulk material [33,34]. In the scope of linearly elastic material, the local coordinate system y is utilized to describe PUCs in the global coordinate system x , shown in Fig. 1. It can be clearly seen that two kinds of PUCs are periodically arranged in different parts of the bulk material.

PUCs are defined in the local coordinate system \mathbf{y} . The elastic property $\mathbf{E}^e(\mathbf{x})$ is \mathbf{y} -periodic function in the global coordinate system \mathbf{x} . The parameter ε is the aspect ratio of the sizes between material unit cells and the bulk material, which is far less than 1. In this case, the displacement field inside PUCs can be characterized by the asymptotic expansion theory. For numerical simplicity, only the first-order term of the small parameter expansion is considered. The homogenized effective elasticity tensor \mathbf{E}^H of the bulk material is calculated by the volume integral in PUCs:

$$E_{ijkl}^H = \frac{1}{|Y|} \int_Y E_{pqrs} (\varepsilon_{pq}^{0(ij)} - \varepsilon_{pq}^{*(ij)}) (\varepsilon_{rs}^{0(kl)} - \varepsilon_{rs}^{*(kl)}) dY \quad (i, j, k, l = 1, 2, \dots, d) \quad (1)$$

where $|Y|$ denotes the area in 2D or the volume in 3D of PUCs. The term $\varepsilon_{pq}^{0(ij)}$ denotes the initial unit test strains which contains six kinds of linearly independent test strains in the 3D scenario, namely $(1, 0, 0, 0, 0, 0)^T$, $(0, 1, 0, 0, 0, 0)^T$, $(0, 0, 1, 0, 0, 0)^T$, $(0, 0, 0, 1, 0, 0)^T$, $(0, 0, 0, 0, 1, 0)^T$ and $(0, 0, 0, 0, 0, 1)^T$. The unknown strain field $\varepsilon_{pq}^{*(ij)}$ induced by the unit test strain is obtained by solving the following linear elasticity equilibrium equation with \mathbf{y} -periodic boundary conditions in PUCs:

$$\int_Y E_{ijpq} \varepsilon_{pq}^{*(kl)} \frac{\partial v_i}{\partial y_j} dY = \int_Y E_{ijpq} \varepsilon_{pq}^{0(kl)} \frac{\partial v_i}{\partial y_j} dY \quad \forall v_i \in H_{per}(Y, \mathbf{R}^3) \quad (2)$$

where the term v_i is the virtual displacement field, which belongs to the admissible displacement space $H_{per}(Y, \mathbf{R}^3)$ with \mathbf{y} -periodicity. In the finite element analysis, PUCs are assumed to use a mesh of *NE* finite elements. The homogenized effective elasticity tensor \mathbf{E}^H can be reformulated as the sum of the integration over finite elements, as given in the following equation:

$$E_{ijkl}^H = \frac{1}{|Y|} \sum_{e=1}^{NE} (\mathbf{u}_e^{0(ij)} - \mathbf{u}_e^{*(ij)})^T \mathbf{k}_e (\mathbf{u}_e^{0(kl)} - \mathbf{u}_e^{*(kl)}) \quad (3)$$

where $\mathbf{u}_e^{*(ij)}$ is the unknown element displacements, and \mathbf{k}_e is the element stiffness matrix.

In the EBHM, the initial unit test strains are directly imposed on the boundaries of PUCs. The induced strain field in PUCs corresponds to the superimposed strain field $(\varepsilon_{pq}^{0(ij)} - \varepsilon_{pq}^{*(ij)})$ in Eq. (1), which is denoted by $\varepsilon_{pq}^{Id(ij)}$. Hence, Eq. (3) would be transformed into a new form in terms of elementary mutual energies [19] by the induced displacement field in PUCs, given as:

$$E_{ijkl}^H = \frac{1}{|Y|} \sum_{e=1}^{NE} Q_{ijkl}^e = \frac{1}{|Y|} \sum_{e=1}^{NE} (\mathbf{u}_e^{Id(ij)})^T \mathbf{k}_e \mathbf{u}_e^{Id(kl)} \quad (4)$$

where \mathbf{u}_e^{Id} denotes the corresponding induced element displacements, and Q_{ijkl}^e stands for the elementary mutual energy. It is noted that the effective elasticity properties are interpreted as the summation of elastic energies of PUCs [19,57]. The homogenized elastic tensor \mathbf{E}^H is expanded as:

$$\mathbf{E}^H = \begin{bmatrix} E_{1111}^H & E_{1122}^H & E_{1133}^H & E_{1112}^H & E_{1123}^H & E_{1131}^H \\ E_{2211}^H & E_{2222}^H & E_{2233}^H & E_{2212}^H & E_{2223}^H & E_{2231}^H \\ E_{3311}^H & E_{3322}^H & E_{3333}^H & E_{3312}^H & E_{3323}^H & E_{3331}^H \\ E_{1211}^H & E_{1222}^H & E_{1233}^H & E_{1212}^H & E_{1223}^H & E_{1231}^H \\ E_{2311}^H & E_{2322}^H & E_{2333}^H & E_{2312}^H & E_{2323}^H & E_{2331}^H \\ E_{3111}^H & E_{3122}^H & E_{3133}^H & E_{3112}^H & E_{3123}^H & E_{3131}^H \end{bmatrix} \quad (5)$$

3. 3D energy-based homogenization method

In the EBHM, the average stress and strain theorems are employed to evaluate the elementary mutual energies. The key principle of the EBHM lies in developing the 3D periodic boundary formulation [58]. Here, the 3D periodic boundary formulation in EBHM is developed and elaborated from the following three factors: 3D periodic boundary

conditions, 3D boundary constraint equations and linearly elastic equilibrium equation.

3.1. 3D periodic boundary conditions

To perfectly maintain the periodicity and continuity conditions of PUCs, the displacement field of PUCs subjected to the given test strain ε^0 can be defined by the summation of the macroscopic displacement field and the periodic fluctuation displacement field \mathbf{u}^{per} [58]:

$$\mathbf{u} = \varepsilon^0 \mathbf{y} + \mathbf{u}^{per} \quad (6)$$

We can find that the periodic fluctuation displacement field are unknown. Hence, Eq. (6) cannot be directly imposed on the opposite boundaries of PUCs to meet the continuity and periodicity. It is necessary to transform the implicit periodic boundary conditions into a number of explicit conditions. In Eq. (6), the displacements on a pair of opposite boundaries in different orientations (i.e., y_1 , y_2 and y_3) of PUCs can be given in a detailed form:

$$\begin{cases} \mathbf{u}^{k+} = \varepsilon^0 \mathbf{y}^{k+} + \mathbf{u}^{per} \\ \mathbf{u}^{k-} = \varepsilon^0 \mathbf{y}^{k-} + \mathbf{u}^{per} \end{cases} \quad (7)$$

where the superscripts $k+$ and $k-$ indicate the normal directions of the pair of two opposite parallel boundaries, respectively. From Eq. (7), it can be easily seen that the periodic fluctuation displacement can be eliminated through the subtraction between two displacements of the opposite boundaries:

$$\mathbf{u}^{k+} - \mathbf{u}^{k-} = \varepsilon^0 (\mathbf{y}^{k+} - \mathbf{y}^{k-}) = \varepsilon^0 \mathbf{w} \quad (8)$$

where $\varepsilon^0 \mathbf{w}$ is the vector of the defined periodic boundary conditions in PUCs. It can be clearly seen that the 3D periodic boundary conditions are evaluated by the initial unit test strain ε^0 as well as the sizes of PUCs. Hence, 3D periodic boundary conditions can be directly imposed on opposite boundaries by constraining displacements of pairs of nodes on the corresponding surfaces, edges and vertices in PUCs.

3.2. 3D boundary constraint equations

Here, an illustration of a 3D PUC is given in Fig. 2, which provides a detailed geometry labels for the PUC including the vertices, edges and surfaces. Firstly, the vertices are labeled from A to H, where the vertex A works as the basis for the rest of vertices. Then, the edges are labeled from I to XII. Finally, the surfaces are numbered from 1 to 6.

When performing finite element analysis, the PUC is discretized by a large number of finite elements. To impose the periodic conditions on boundaries, we define a reasonable classification of nodes in the PUC. The nodes related to the vertices are defined in **Node 1** set. The **Node 2** set contains the nodes located at the edges, while excludes the nodes in **Node 1** set. The nodes located at the surfaces are defined in **Node 3** set as well as excluding the **Node 1** and **Node 2** sets. The rest nodes located at the interior of the PUC are defined in **Node 4** set. The detailed information of the classified sets is provided in Table 1.

According to the initial unit test strains and the dimensions of the PUC in Eq. (8), the 3D periodic boundary conditions can be illustrated by the explicit 3D boundary constraint equations as functions of the displacement difference among the multiple nodes located at the vertices, edges and surfaces in the PUC. At first, the initial unit test strain vector ε^0 contains three normal strains and three shear strains in PUCs, denoted by $\varepsilon^{0(xx)}$, $\varepsilon^{0(yy)}$, $\varepsilon^{0(zz)}$, $\gamma^{0(xy)}$, $\gamma^{0(yz)}$ and $\gamma^{0(xz)}$, respectively. The dimensions of PUCs in all directions are defined as l_x , l_y and l_z . According to the above classification of the nodes, the boundary constraint equations are listed in Tables 2–4, which can be roughly divided into three classes in terms of the vertices, edges and surfaces. The first class of boundary constraint equations \mathbf{w}_0 in Table 2 is evaluated by the displacement difference between the vertex A and other vertices in **Node 1** set. u , v and w denote the displacement of nodes in three

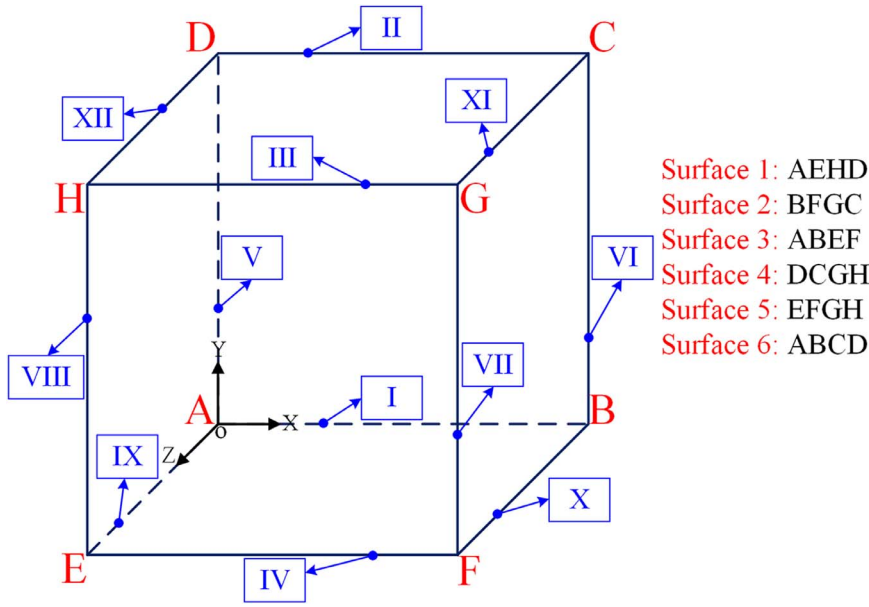


Fig. 2. A 3D PUC.

Table 1
The sets of nodes.

Set	Nodes
Node 1:	Vertex nodes (eight points A, B, ..., H)
Node 2:	Edge nodes (twelve edges I, II, ..., XII excluding nodes in vertices)
Node 3:	Surface nodes (six surfaces 1, 2, ..., 6 excluding nodes in vertices and edges)
Node 4:	The remaining inner nodes in PUCs

directions of PUCs, respectively. The second class of boundary constraint equations defined in the **Node 2** set are listed in Table 3. Three subtypes w_1 , w_2 and w_3 are defined according to the orientations of structural edges. Finally, the third class of boundary constraint equations w_4 developed in **Node 3** set is shown in Table 4, which shows boundary conditions imposed on the surfaces. It should be noted that boundary constraint equations in different node sets are conformed to the same basic principle that the displacement difference between the opposite pairs of nodes realizes the periodicity and continuity conditions.

3.3. Reduced linearly elastic equilibrium equation

Here, it is very suitable to adopt the direct solution scheme [28,57] in the finite element analysis since the above explicit boundary constraint equations can be applied to eliminate some redundant unknowns in the linearly elastic equilibrium equation. Based on the node sets in Table 1, the global displacement vector U can be divided into the following eight components:

Table 2
The first class of boundary constraint equations.

Node 1: w_0			
$\begin{cases} u^B - u^A = l_x \varepsilon^{0}(xx) \\ v^B - v^A = 0 \\ w^B - w^A = 0 \end{cases}$	$\begin{cases} u^C - u^A = l_x \varepsilon^{0}(xx) + l_y \gamma^{0}(xy) \\ v^C - v^A = l_y \varepsilon^{0}(yy) \\ w^C - w^A = 0 \end{cases}$	$\begin{cases} u^D - u^A = l_y \gamma^{0}(xy) \\ v^D - v^A = l_y \varepsilon^{0}(yy) \\ w^D - w^A = 0 \end{cases}$	$\begin{cases} u^E - u^A = l_z \gamma^{0}(xz) \\ v^E - v^A = l_z \gamma^{0}(yz) \\ w^E - w^A = l_z \varepsilon^{0}(zz) \end{cases}$
$\begin{cases} u^F - u^A = l_x \varepsilon^{0}(xx) + l_z \gamma^{0}(xz) \\ v^F - v^A = l_z \gamma^{0}(yz) \\ w^F - w^A = l_z \varepsilon^{0}(zz) \end{cases}$	$\begin{cases} u^G - u^A = l_x \varepsilon^{0}(xx) + l_y \gamma^{0}(xy) + l_z \gamma^{0}(xz) \\ v^G - v^A = l_y \varepsilon^{0}(yy) + l_z \gamma^{0}(yz) \\ w^G - w^A = l_z \varepsilon^{0}(zz) \end{cases}$	$\begin{cases} u^H - u^A = l_y \gamma^{0}(xy) + l_z \gamma^{0}(xz) \\ v^H - v^A = l_y \varepsilon^{0}(yy) + l_z \gamma^{0}(yz) \\ w^H - w^A = l_z \varepsilon^{0}(zz) \end{cases}$	

Table 3
The second class of boundary constraint equations.

Node 2: w_1	Node 2: w_2	Node 2: w_3
$\begin{cases} u^{II} - u^I = l_y \gamma^{0}(xy) \\ v^{II} - v^I = l_y \varepsilon^{0}(yy) \\ w^{II} - w^I = 0 \end{cases}$	$\begin{cases} u^{III} - u^I = l_y \gamma^{0}(xy) + l_z \gamma^{0}(xz) \\ v^{III} - v^I = l_y \varepsilon^{0}(yy) + l_z \gamma^{0}(yz) \\ w^{III} - w^I = l_z \varepsilon^{0}(zz) \end{cases}$	$\begin{cases} u^{IV} - u^I = l_z \gamma^{0}(xz) \\ v^{IV} - v^I = l_z \gamma^{0}(yz) \\ w^{IV} - w^I = l_z \varepsilon^{0}(zz) \end{cases}$
$\begin{cases} u^{VI} - u^V = l_x \varepsilon^{0}(xx) \\ v^{VI} - v^V = 0 \\ w^{VI} - w^V = 0 \end{cases}$	$\begin{cases} u^{VII} - u^V = l_x \varepsilon^{0}(xx) + l_z \gamma^{0}(xz) \\ v^{VII} - v^V = l_z \gamma^{0}(yz) \\ w^{VII} - w^V = l_z \varepsilon^{0}(zz) \end{cases}$	$\begin{cases} u^{VIII} - u^V = l_z \gamma^{0}(xz) \\ v^{VIII} - v^V = l_z \gamma^{0}(yz) \\ w^{VIII} - w^V = l_z \varepsilon^{0}(zz) \end{cases}$
$\begin{cases} u^X - u^{IX} = l_x \varepsilon^{0}(xx) \\ v^X - v^{IX} = 0 \\ w^X - w^{IX} = 0 \end{cases}$	$\begin{cases} u^{XI} - u^{IX} = l_x \varepsilon^{0}(xx) + l_y \gamma^{0}(xy) \\ v^{XI} - v^{IX} = l_y \varepsilon^{0}(yy) \\ w^{XI} - w^{IX} = 0 \end{cases}$	$\begin{cases} u^{XII} - u^{IX} = l_y \gamma^{0}(xy) \\ v^{XII} - v^{IX} = l_y \varepsilon^{0}(yy) \\ w^{XII} - w^{IX} = 0 \end{cases}$

Table 4
The third class of boundary constraint equations.

Node 3: w_4		
$\begin{cases} u^2 - u^1 = l_x \varepsilon^{0}(xx) \\ v^2 - v^1 = 0 \\ w^2 - w^1 = 0 \end{cases}$	$\begin{cases} u^4 - u^3 = l_y \gamma^{0}(xy) \\ v^4 - v^3 = l_y \varepsilon^{0}(yy) \\ w^4 - w^3 = 0 \end{cases}$	$\begin{cases} u^6 - u^5 = l_z \gamma^{0}(xz) \\ v^6 - v^5 = l_z \gamma^{0}(yz) \\ w^6 - w^5 = l_z \varepsilon^{0}(zz) \end{cases}$

- U_1 : the displacement vector of nodes located at the vertices in PUCs, and it is defined by the imposed initial unit test strains.
- U_2 : the unknown displacement vector of the interior nodes in PUCs.
- U_3 : the displacement vector of nodes located at the edges I, V and IX in PUCs.

- \mathbf{U}_4 : the displacement vector of nodes located at the edges II, VI and X in PUCs.
- \mathbf{U}_5 : the displacement vector of nodes located at the edges III, VII and XI in PUCs.
- \mathbf{U}_6 : the displacement vector of nodes located at the edges IV, VIII and XII in PUCs.
- \mathbf{U}_7 : the displacement vector of nodes located at the surfaces 1, 3 and 5 in PUCs.
- \mathbf{U}_8 : the displacement vector of nodes located at the surfaces 2, 4 and 6 in PUCs.

Note that, \mathbf{U}_1 denotes the displacement vector of the vertices in **Node 1** set. The displacement vector of the interior nodes in **Node 4** set is denoted by \mathbf{U}_2 . The displacement vector of the nodes in **Node 2** set is divided into four subtypes according to the edges, namely \mathbf{U}_3 , \mathbf{U}_4 , \mathbf{U}_5 and \mathbf{U}_6 . The \mathbf{U}_3 vector works as the basis for the rest vectors \mathbf{U}_4 , \mathbf{U}_5 and \mathbf{U}_6 to define the displacement difference between the pairs of nodes located at the opposite edges. The displacement vectors \mathbf{U}_7 and \mathbf{U}_8 correspond to the nodes located at surfaces in **Node 3** set. Accordingly, the equilibrium equation can be expanded as a new form:

$$\begin{bmatrix} \mathbf{K}_{11} & \mathbf{K}_{12} & \mathbf{K}_{13} & \mathbf{K}_{14} & \mathbf{K}_{15} & \mathbf{K}_{16} & \mathbf{K}_{17} & \mathbf{K}_{18} \\ \mathbf{K}_{21} & \mathbf{K}_{22} & \mathbf{K}_{23} & \mathbf{K}_{24} & \mathbf{K}_{25} & \mathbf{K}_{26} & \mathbf{K}_{27} & \mathbf{K}_{28} \\ \mathbf{K}_{31} & \mathbf{K}_{32} & \mathbf{K}_{33} & \mathbf{K}_{34} & \mathbf{K}_{35} & \mathbf{K}_{36} & \mathbf{K}_{37} & \mathbf{K}_{38} \\ \mathbf{K}_{41} & \mathbf{K}_{42} & \mathbf{K}_{43} & \mathbf{K}_{44} & \mathbf{K}_{45} & \mathbf{K}_{46} & \mathbf{K}_{47} & \mathbf{K}_{48} \\ \mathbf{K}_{51} & \mathbf{K}_{52} & \mathbf{K}_{53} & \mathbf{K}_{54} & \mathbf{K}_{55} & \mathbf{K}_{56} & \mathbf{K}_{57} & \mathbf{K}_{58} \\ \mathbf{K}_{61} & \mathbf{K}_{62} & \mathbf{K}_{63} & \mathbf{K}_{64} & \mathbf{K}_{65} & \mathbf{K}_{66} & \mathbf{K}_{67} & \mathbf{K}_{68} \\ \mathbf{K}_{71} & \mathbf{K}_{72} & \mathbf{K}_{73} & \mathbf{K}_{74} & \mathbf{K}_{75} & \mathbf{K}_{76} & \mathbf{K}_{77} & \mathbf{K}_{78} \\ \mathbf{K}_{81} & \mathbf{K}_{82} & \mathbf{K}_{83} & \mathbf{K}_{84} & \mathbf{K}_{85} & \mathbf{K}_{86} & \mathbf{K}_{87} & \mathbf{K}_{88} \end{bmatrix} \begin{bmatrix} \mathbf{U}_1 \\ \mathbf{U}_2 \\ \mathbf{U}_3 \\ \mathbf{U}_4 \\ \mathbf{U}_5 \\ \mathbf{U}_6 \\ \mathbf{U}_7 \\ \mathbf{U}_8 \end{bmatrix} = \begin{bmatrix} \mathbf{F}_1 \\ \mathbf{F}_2 \\ \mathbf{F}_3 \\ \mathbf{F}_4 \\ \mathbf{F}_5 \\ \mathbf{F}_6 \\ \mathbf{F}_7 \\ \mathbf{F}_8 \end{bmatrix} \quad (9)$$

The first row of the global stiffness matrix defined in Eq. (9) can be eliminated due to the fact that \mathbf{U}_1 is known according to the first class of boundary constraint equations \mathbf{w}_0 . Because PUCs maintain the periodicity and continuity assumption, the load vector in PUCs yields $\mathbf{F}_2 = 0$, $\mathbf{F}_3 + \mathbf{F}_4 + \mathbf{F}_5 + \mathbf{F}_6 = 0$ and $\mathbf{F}_7 + \mathbf{F}_8 = 0$. Meanwhile, the displacement vector \mathbf{U}_3 with respect to \mathbf{U}_4 , \mathbf{U}_5 , and \mathbf{U}_6 satisfies boundary constraint equations \mathbf{w}_1 , \mathbf{w}_2 and \mathbf{w}_3 respectively. The displacement vectors \mathbf{U}_7 and \mathbf{U}_8 also meet the corresponding conditions \mathbf{w}_4 . Thus, the constraint equations of PUCs are developed in terms of both the force and displacement, given as:

$$\begin{cases} \mathbf{F}_2 = 0 \\ \mathbf{F}_3 + \mathbf{F}_4 + \mathbf{F}_5 + \mathbf{F}_6 = 0 \\ \mathbf{F}_7 + \mathbf{F}_8 = 0 \\ \mathbf{U}_4 = \mathbf{U}_3 + \mathbf{w}_1 \\ \mathbf{U}_5 = \mathbf{U}_3 + \mathbf{w}_2 \\ \mathbf{U}_6 = \mathbf{U}_3 + \mathbf{w}_3 \\ \mathbf{U}_8 = \mathbf{U}_7 + \mathbf{w}_4 \end{cases} \quad (10)$$

Substituting Eq. (10) into Eq. (9), the elastic equilibrium equation defined in Eq. (9) can be transformed into a much more compact form, as follows:

$$\mathbf{K}_r \mathbf{U}_r = \mathbf{F}_r \quad (11)$$

where,

$$\begin{cases} \mathbf{K}_r = \begin{bmatrix} \mathbf{K}_{22} & \sum_{j=3}^6 \mathbf{K}_{2j} & \sum_{j=7}^8 \mathbf{K}_{2j} \\ \text{sym} & \sum_{i=3}^6 \sum_{j=3}^6 \mathbf{K}_{ij} & \sum_{i=3}^6 \sum_{j=7}^8 \mathbf{K}_{ij} \\ \text{sym} & \text{sym} & \sum_{i=7}^8 \sum_{j=7}^8 \mathbf{K}_{ij} \end{bmatrix} \\ \mathbf{U}_r = \begin{bmatrix} \mathbf{U}_2 \\ \mathbf{U}_3 \\ \mathbf{U}_7 \end{bmatrix} \\ \mathbf{F}_r = - \begin{bmatrix} \mathbf{K}_{21} \\ \sum_{i=3}^6 \mathbf{K}_{i1} \\ \mathbf{K}_{71} + \mathbf{K}_{81} \end{bmatrix} \mathbf{U}_1 - \begin{bmatrix} \mathbf{K}_{24} \\ \sum_{i=3}^6 \mathbf{K}_{i4} \\ \mathbf{K}_{74} + \mathbf{K}_{84} \end{bmatrix} \mathbf{w}_1 \\ - \begin{bmatrix} \mathbf{K}_{25} \\ \sum_{i=3}^6 \mathbf{K}_{i5} \\ \mathbf{K}_{75} + \mathbf{K}_{85} \end{bmatrix} \mathbf{w}_2 - \begin{bmatrix} \mathbf{K}_{26} \\ \sum_{i=3}^6 \mathbf{K}_{i6} \\ \mathbf{K}_{76} + \mathbf{K}_{86} \end{bmatrix} \mathbf{w}_3 - \begin{bmatrix} \mathbf{K}_{28} \\ \sum_{i=3}^6 \mathbf{K}_{i8} \\ \mathbf{K}_{78} + \mathbf{K}_{88} \end{bmatrix} \mathbf{w}_4 \end{cases} \quad (12)$$

Compared with Eq. (9), the global stiffness matrix \mathbf{K} , global displacement field \mathbf{U} and global load vector \mathbf{F} are reduced to \mathbf{K}_r , \mathbf{U}_r and \mathbf{F}_r in Eq. (11), respectively. The computational scales of equilibrium equation can be reduced to an extent. Hence, the direct solution scheme may be beneficial to improve the efficiency of numerical analysis by eliminating some redundant unknowns in Eq. (9), like \mathbf{U}_4 , \mathbf{U}_5 , \mathbf{U}_6 and \mathbf{U}_8 .

4. Design of 3D micro-structured materials

Material effective properties are evaluated by the EBHM according to the topologies of PUCs, while topology optimization can be applied to seek the best configurations of PUCs. Hence, an effective design method is developed to seek for the PUCs with extreme effective properties.

4.1. Parametric level set-based topological shape optimization

In the LSM, structural design boundary is embedded implicitly as the zero-contour (in 2D) or the iso-surface (in 3D) of a higher-dimensional level set function (LSF) [15]. As shown in Fig. 3, a 2D structure is illustrated by a 3D LSF, where the reference domain $D \subset \mathbb{R}^d$ ($d = 2 \text{ or } 3$) includes all admissible shapes Ω ($\Omega \subset D$), defined as:

$$\begin{cases} \Phi(\mathbf{x}) > 0, \forall \mathbf{x} \in \Omega \setminus \Gamma(\text{solid}) \\ \Phi(\mathbf{x}) = 0, \forall \mathbf{x} \in \Gamma \cap D(\text{boundary}) \\ \Phi(\mathbf{x}) < 0, \forall \mathbf{x} \in D \setminus \Omega(\text{void}) \end{cases} \quad (13)$$

where Ω is structural design domain and Γ denotes structural boundary. By introducing a pseudo-time t into the LSF, its dynamic form $\Phi(\mathbf{x}, t)$ can be obtained. Through differentiating $\Phi(\mathbf{x}, t) = 0$ on both sides with respect to time variable t , the dynamic deformation of structural boundary is transformed into changing the zero level set of LSFs in time, which can be formulated by the first-order H-J PDEs [15]:

$$\frac{\partial \Phi(\mathbf{x}, t)}{\partial t} - v_n |\nabla \Phi(\mathbf{x}, t)| = 0 \quad (14)$$

where v_n is the normal velocity field at structural boundary. Hence, moving structural boundary by the normal velocity field can be

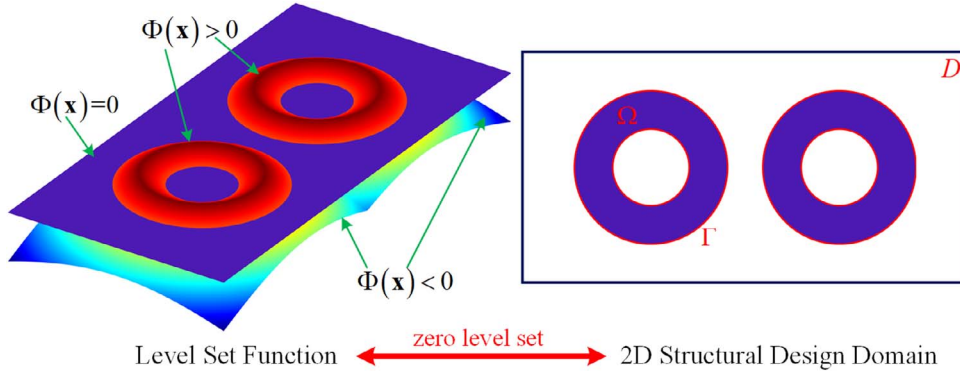


Fig. 3. 3D LSF and 2D structural design domain.

regarded as finding the feasible solution of H-J PDEs. However, the numerical calculation of the direct solving of the H-J PDEs is relatively complex [16,17].

In the PLSM, the LSF is approximately calculated by a set of CSRBFs [59] at a number of knots over the design domain, as:

$$\Phi(\mathbf{x}, t) = \varphi(\mathbf{x})^T \alpha(t) = \sum_{i=1}^N \phi_i(\mathbf{x}) \alpha_i(t) \quad (15)$$

where the series of CSRBFs are formulated as a vector at each knot, given by:

$$\varphi(\mathbf{x}) = [\phi_1(\mathbf{x}) \ \phi_2(\mathbf{x}) \ \cdots \ \phi_N(\mathbf{x})]^T \quad (16)$$

where N is the total number of nodes in the level set grid. The CSRBFs with C2 continuity [59] are employed here:

$$\phi(\mathbf{r}) = (\max(0, 1 - \mathbf{r}))^4 (4\mathbf{r} + 1) \quad (17)$$

where \mathbf{r} denotes the sizes of influence domain of basis function at the knot in design domain. Hence, the CSRBFs are only dependent on the spatial locations of knots, and the expansion coefficients in Eq. (15) are evolved gradually with time, given as:

$$\alpha(t) = [\alpha_1(t) \ \alpha_2(t) \ \cdots \ \alpha_N(t)]^T \quad (18)$$

Substituting Eq. (15) into Eq. (14), the H-J PDE is transformed into a time-space independent form, as:

$$\varphi(\mathbf{x})^T \frac{d\alpha(t)}{dt} - v_n |(\nabla \varphi(\mathbf{x}))^T \alpha(t)| = 0 \quad (19)$$

and the normal velocity v_n can be given by:

$$v_n = \frac{\varphi(\mathbf{x})^T}{|(\nabla \varphi(\mathbf{x}))^T \alpha(t)|} \cdot \frac{d\alpha(t)}{dt} \quad (20)$$

From Eq. (20), it can be seen that the normal velocity field v_n is naturally extended to the whole design domain, and the original H-J PDE is transformed into a series of ordinary differential equations only with a set of unknown expansion coefficients. Since there is no need to directly solve the H-J PDE, some complex numerical implementations are eliminated [16,17]. The PLSM will perfectly serve for the optimization of structures [49,50].

4.2. Optimization model

In this study, the intention of micro-structured materials design is to seek the best configurations of PUCs with the maximum bulk modulus and maximum shear modulus. The definition of the optimization model is the remaining part of the problem statement here:

$$\text{find: } \alpha = [\alpha_1 \ \alpha_2 \ \cdots \ \alpha_N]$$

$$\text{Maximize: } J(\mathbf{u}, \Phi) = \sum_{i,j,k,l=1}^d \eta_{ijkl} E_{ijkl}^H(\alpha)$$

$$\text{Subjectto: } \begin{cases} V(\Phi(\alpha)) = \int_{\Omega} H(\Phi(\alpha)) d\Omega - V_{\max} \leq 0 \\ a(\mathbf{u}, \mathbf{v}, \Phi) = l(\mathbf{v}, \Phi) \ \forall \mathbf{v} \in H_{per}(\Omega, \mathbf{R}^3) \\ \alpha^L \leq \alpha_n \leq \alpha^U \ (n = 1, 2, \dots, N) \end{cases} \quad (21)$$

where α denotes the vector of design variables. α^L and α^U are the lower and upper bounds of design variables, respectively. J is the objective function defined by a combination of the homogenized elastic tensor \mathbf{E}^H and the weight factor η_{ijkl} , in which the former is computed by the EBHM in Eq. (6). V is the volume constraint with an upper bound of V_{\max} . H is the Heaviside function which serves as a characteristic function [16], given as:

$$H(\Phi) = \begin{cases} \eta, & \Phi < -\Delta \\ \frac{3(1-\eta)}{4} \left(\frac{\Phi}{\Delta} - \frac{\Phi^3}{3\Delta^3} \right) + \frac{1+\eta}{2}, & -\Delta \leq \Phi \leq \Delta \\ 1, & \Phi > \Delta \end{cases} \quad (22)$$

where η is a small positive number to avoid singularity of the numerical process, and Δ describes the width for numerical approximation of H . The elastic equilibrium equation is stated in the weak variational form, in which the bilinear energy term a and the linear load form l can be written as:

$$\begin{cases} a(\mathbf{u}, \mathbf{v}, \Phi) = \int_{\Omega} \varepsilon_{ij}(\mathbf{u}) E_{ijkl}(\mathbf{v}) H(\Phi) d\Omega \\ l(\mathbf{v}, \Phi) = \int_{\Omega} \varepsilon_{ij}(\mathbf{u}^0) E_{ijkl}(\mathbf{v}) H(\Phi) d\Omega \end{cases} \quad (23)$$

where \mathbf{v} is the virtual displacement field, which belongs to the kinematically admissible displacement space.

4.3. Design sensitivity analysis

In this study, the optimization model is solved by the well-established optimization algorithm, like the OC. The first-order derivatives of the objective and constraint functions associated with the design variables are required. The derivatives of the objective function can be derived by:

$$\frac{\partial J}{\partial \alpha} = \sum_{i,j,k,l=1}^d \left(\eta_{ijkl} \frac{\partial E_{ijkl}^H}{\partial \alpha} \right) \quad (24)$$

where the derivative of the effective homogenized elasticity tensor \mathbf{E}^H with respect to time is given by:

$$\frac{dE_{ijkl}^H}{dt} = \frac{1}{|\mathbf{Y}|} \int_{\Omega} E_{pqrs} (\varepsilon_{pq}^{0(ij)} - \varepsilon_{pq}^{*(ij)}) (\varepsilon_{rs}^{0(kl)} - \varepsilon_{rs}^{*(kl)}) v_n |\nabla \Phi| \delta(\Phi) d\Omega \quad (25)$$

where $\delta(\cdot)$ is the partial derivative of the Heaviside function H , namely the Dirac function [60]. Recalling the normal velocity field v_n given in

Eq. (20), and substituting it into Eq. (25), it yields:

$$\frac{dE_{ijkl}^H}{dt} = \frac{1}{|Y|} \int_D E_{pqrs} (\epsilon_{pq}^{0(ij)} - \epsilon_{pq}^{*(ij)}) (\epsilon_{rs}^{0(kl)} - \epsilon_{rs}^{*(kl)}) \left(\varphi(\mathbf{x})^T \frac{d\alpha(t)}{dt} \right) \delta(\Phi) d\Omega \quad (26)$$

Because the expansion coefficient α is only dependent on time, the form in Eq. (26) can be expanded as:

$$\frac{dE_{ijkl}^H}{dt} = \frac{1}{|Y|} \left\{ \int_D E_{pqrs} (\epsilon_{pq}^{0(ij)} - \epsilon_{pq}^{*(ij)}) (\epsilon_{rs}^{0(kl)} - \epsilon_{rs}^{*(kl)}) \varphi(\mathbf{x})^T \delta(\Phi) d\Omega \right\} \frac{d\alpha(t)}{dt} \quad (27)$$

On the other hand, the derivative of the effective elasticity tensor with respect to the time variable can be derived based on the chain rule:

$$\frac{dE_{ijkl}^H}{dt} = \frac{\partial E_{ijkl}^H}{\partial \alpha} \cdot \frac{d\alpha(t)}{dt} \quad (28)$$

By comparing Eqs. (27) and (28), the derivatives of the homogenized elastic tensor E^H with respect to expansion coefficients are given by:

$$\frac{\partial E_{ijkl}^H}{\partial \alpha} = \frac{1}{|Y|} \int_D E_{pqrs} (\epsilon_{pq}^{0(ij)} - \epsilon_{pq}^{*(ij)}) (\epsilon_{rs}^{0(kl)} - \epsilon_{rs}^{*(kl)}) \varphi(\mathbf{x})^T \delta(\Phi) d\Omega \quad (29)$$

Similarly, the derivatives of the volume constraint with regard to design variables can be derived as:

$$\frac{\partial V}{\partial \alpha} = \frac{1}{|Y|} \int_D \varphi(\mathbf{x})^T \delta(\Phi) d\Omega \quad (30)$$

5. Numerical implementations

In the proposed design method, the OC algorithm is applied to update design variables because it is suitable for the optimization problem with a large number of design variables but the single constraint. A heuristic updating scheme of the OC is stated as:

$$\alpha_j^{k+1} = \begin{cases} \max\{(1-m)\alpha_j^k, \alpha^L\}, & \text{if } (D_j^k)^\zeta \alpha_j^k \leq \max\{(1-m)\alpha_j^k, \alpha^L\} \\ (D_j^k)^\zeta \alpha_j^k, & \text{if } \begin{cases} \max\{(1-m)\alpha_j^k, \alpha^L\} < (D_j^k)^\zeta \alpha_j^k < \\ \min\{(1+m)\alpha_j^k, \alpha^U\} \end{cases} \\ \min\{(1+m)\alpha_j^k, \alpha^U\}, & \text{if } \min\{(1+m)\alpha_j^k, \alpha^U\} \leq (D_j^k)^\zeta \alpha_j^k \end{cases} \quad (31)$$

where m and ζ are the move limit and the damping factor, respectively. The term D_j^k stands for the updating factor, which is dependent on the sensitivities of the objective and constraint functions:

$$D_j^k = \frac{\partial E_{ijkl}^H}{\partial \alpha_j^k} / \left(\max \left(\mu, \Lambda^k \frac{\partial V}{\partial \alpha_j^k} \right) \right) \quad (32)$$

where μ is a very small positive constant to avoid numerical singularity, and the Lagrange multiplier Λ can be updated by a bi-sectioning algorithm [9].

The whole flowchart of the proposed design method for the 3D micro-structured materials is shown in Fig. 4. It mainly contains two parts. The first part works as the basic framework of the design model by the PLSM, which is utilized to optimize the configurations of PUCs based on the first-order derivatives of the objective and constraint functions. The second part corresponds to the development of the 3D EBHM which is applied to evaluate effective properties of micro-structures based on the 3D periodic boundary formulation.

6. Numerical examples

In this section, numerical examples are presented to demonstrate the validity of the 3D EBHM and the positive features of the proposed

design method. In all examples, the Young's moduli for the solid material and void phase are defined as 1 and 0.0001, respectively. The Poisson's ratio is set as 0.3. For simplicity, the dimensions of PUCs are defined as $1 \times 1 \times 1$, which use a mesh of $20 \times 20 \times 20$ eight-node cubic finite elements. The 'ersatz material' model is utilized to approximately calculate the properties of those elements cut by the moving boundary in the finite element analysis [17]. The move limit m is defined as 0.001 and the damp factor ζ is fixed to be 0.3. The optimization will be terminated when the difference of the objective between two successive steps is less than 10^{-5} or the maximum 150 iteration steps are reached. For numerical simplicity, the CSRBFs mesh is consistent with the finite element mesh.

6.1. Test of the 3D EBHM

In this section, the validity of the 3D EBHM is presented by its comparison with the 3D NHM. Both of these two methods are applied to evaluate homogenized effective elasticity tensors of three PUCs in Fig. 5. The first one is fully filled with solid materials, and some holes are uniformly distributed in the latter. In Table 5, the corresponding numerical results obtained by two methods are provided. It can be clearly seen that the effective elastic tensors E^H are exactly the same for these two methods. Hence, the validity of the 3D EBHM developed in Section 3 is demonstrated.

In terms of the computational efficiency of the developed 3D EBHM, it would be observed that the elimination of redundant unknowns in Eq. (11) will reduce the computational scales of the global stiffness, displacement and load matrices. However, note that, only the specific degrees of freedom (DOFs) located at the vertices, edges and surfaces of PUCs are not considered when solving Eq. (9), since boundary constraint equations are developed on the boundaries of PUCs. The majority of DOFs are located in the interior of PUCs, which are still required to solve the equilibrium equation. Hence, the reduction of computing costs will be limited.

Nevertheless, it is worth noticing that the 3D EBHM with the 3D periodic boundary formulation and the direct solution scheme may be beneficial to improve the efficiency of the finite element analysis. Moreover, the development of the 3D periodic boundary formulation is the key contribution in this work to evaluate 3D effective properties based on the average stress and strain theorems, which can avoid the complex derivations of the asymptotic theory and the related numerical solution schemes [33–35].

6.2. 3D micro-structured materials with maximum bulk modulus

In this section, the proposed design method is applied for maximizing the bulk modulus of the 3D micro-structured materials by evolving configurations of PUCs. The objective function is defined as:

$$J(\mathbf{u}, \Phi) = \sum_{i,k=1}^3 E_{ijkl}^H (i = j \text{ \& } k = l) \quad (33)$$

Here, the effect of the volume fraction on effective elasticity properties is discussed. Three kinds of volume fraction constraints are defined as 0.4, 0.45 and 0.5, respectively. As shown in Fig. 6, two initializations of PUCs are displayed. In initialization 1, some holes are uniformly distributed, while a PUC fully filled with materials is used in initialization 2 to illustrate the positive features of the PLSM. The design of 3D material microstructures to gain maximum bulk modulus will be performed under four cases. Cases 1–3 correspond to the combinations of the initialization 1 with volume constraints 0.4, 0.45, and 0.5, respectively, while the initialization 2 and volume constraint 0.4 are employed in case 4.

After implementing the proposed method, the optimized results of four cases are listed in Table 6, including the optimized topologies of PUCs, $3 \times 3 \times 3$ repetitive PUCs, corresponding homogenized elastic

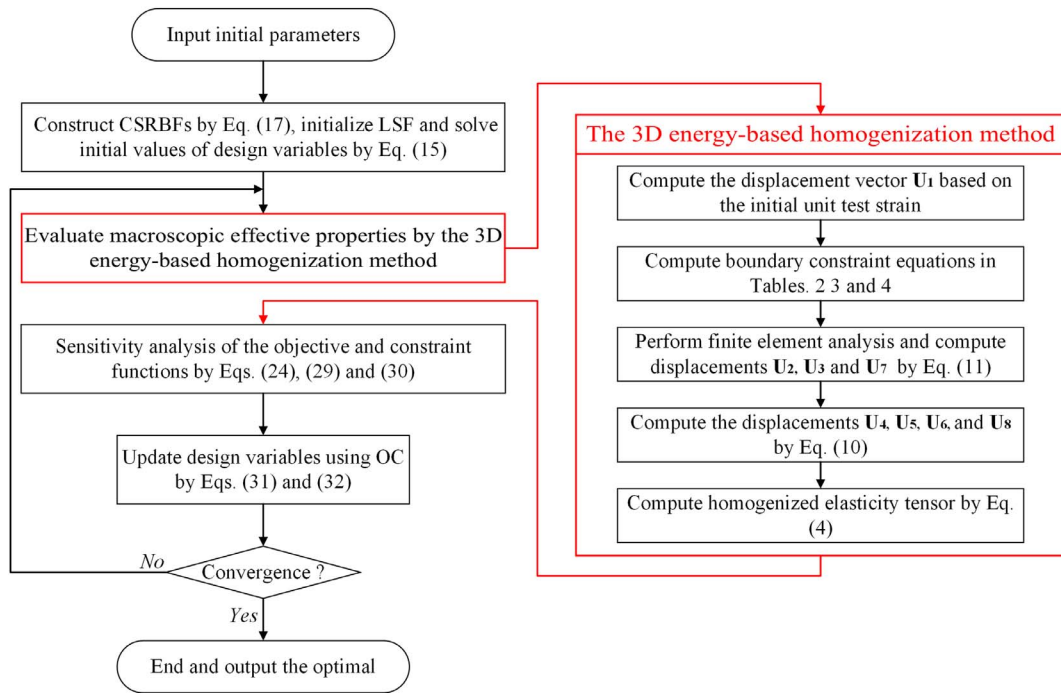


Fig. 4. The flowchart of the proposed design method.

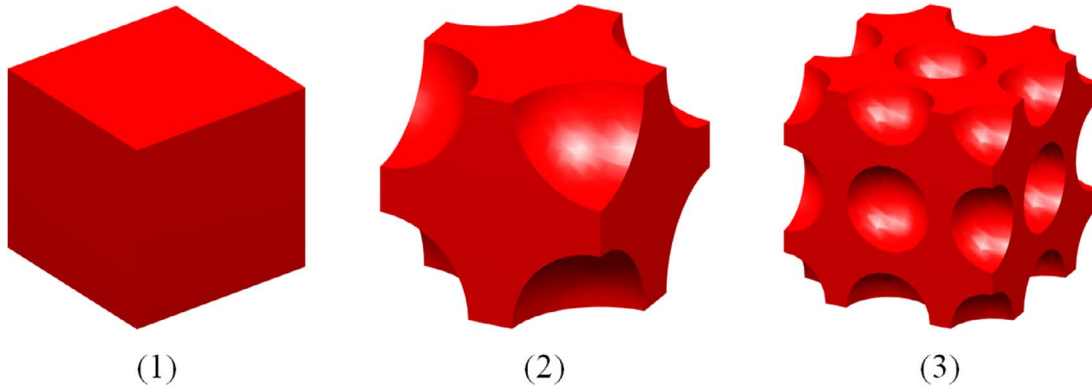


Fig. 5. Three PUCs.

Table 5
Numerical results obtained by the 3D EBHM and 3D NHM.

PUC	3D EBHM	3D NHM
1	$\begin{bmatrix} 1.3462 & 0.5769 & 0.5769 & 0 & 0 & 0 \\ 0.5769 & 1.3462 & 0.5769 & 0 & 0 & 0 \\ 0.5769 & 0.5769 & 1.3462 & 0 & 0 & 0 \\ 0 & 0 & 0 & 0.38462 & 0 & 0 \\ 0 & 0 & 0 & 0 & 0.38462 & 0 \\ 0 & 0 & 0 & 0 & 0 & 0.38462 \end{bmatrix}$	$\begin{bmatrix} 1.3462 & 0.5769 & 0.5769 & 0 & 0 & 0 \\ 0.5769 & 1.3462 & 0.5769 & 0 & 0 & 0 \\ 0.5769 & 0.5769 & 1.3462 & 0 & 0 & 0 \\ 0 & 0 & 0 & 0.38462 & 0 & 0 \\ 0 & 0 & 0 & 0 & 0.38462 & 0 \\ 0 & 0 & 0 & 0 & 0 & 0.38462 \end{bmatrix}$
2	$\begin{bmatrix} 0.7608 & 0.2613 & 0.2613 & 0 & 0 & 0 \\ 0.2613 & 0.7608 & 0.2613 & 0 & 0 & 0 \\ 0.2613 & 0.2613 & 0.7608 & 0 & 0 & 0 \\ 0 & 0 & 0 & 0.20956 & 0 & 0 \\ 0 & 0 & 0 & 0 & 0.20956 & 0 \\ 0 & 0 & 0 & 0 & 0 & 0.20956 \end{bmatrix}$	$\begin{bmatrix} 0.7608 & 0.2613 & 0.2613 & 0 & 0 & 0 \\ 0.2613 & 0.7608 & 0.2613 & 0 & 0 & 0 \\ 0.2613 & 0.2613 & 0.7608 & 0 & 0 & 0 \\ 0 & 0 & 0 & 0.20956 & 0 & 0 \\ 0 & 0 & 0 & 0 & 0.20956 & 0 \\ 0 & 0 & 0 & 0 & 0 & 0.20956 \end{bmatrix}$
3	$\begin{bmatrix} 0.7878 & 0.2744 & 0.2744 & 0 & 0 & 0 \\ 0.2744 & 0.7878 & 0.2744 & 0 & 0 & 0 \\ 0.2744 & 0.2744 & 0.7878 & 0 & 0 & 0 \\ 0 & 0 & 0 & 0.21884 & 0 & 0 \\ 0 & 0 & 0 & 0 & 0.21884 & 0 \\ 0 & 0 & 0 & 0 & 0 & 0.21884 \end{bmatrix}$	$\begin{bmatrix} 0.7878 & 0.2744 & 0.2744 & 0 & 0 & 0 \\ 0.2744 & 0.7878 & 0.2744 & 0 & 0 & 0 \\ 0.2744 & 0.2744 & 0.7878 & 0 & 0 & 0 \\ 0 & 0 & 0 & 0.21884 & 0 & 0 \\ 0 & 0 & 0 & 0 & 0.21884 & 0 \\ 0 & 0 & 0 & 0 & 0 & 0.21884 \end{bmatrix}$

tensor \mathbf{E}^H and the optimal objective J . It can be clearly seen that the optimal configurations of the PUCs with maximum bulk modulus obtained by the proposed method are consistent with those in references

[21,22]. Hence, the validity of the proposed method for 3D micro-structured materials design is demonstrated, as well as the validity of the developed 3D EBHM. Meanwhile, it can be observed that all the

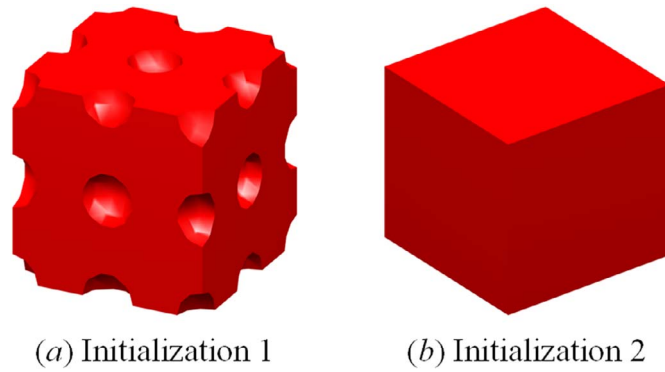


Fig. 6. Initializations of the PUC.

optimized 3D micro-structured topologies are characterized with smooth geometries and clear interfaces, shown in the second and third columns of Table 6. Therefore, there is no need to employ the post-processing mechanism to smooth structural boundaries for the latter manufacturing phase. It is known that introducing extra schemes would make the result deviate away from the optimum, and the performance

of the optimal design would degenerate after the post-processing. Compared with material density interpolation model, the implicit boundary model of the PLSM is much more suitable for the representation of geometrical features. To further illustrate the positive geometrical features, the cross-sectional views of the optimized PUCs in four cases are provided in Table 7. The geometrical details in PUCs with smooth boundaries and clear interfaces can be seen clearly. Hence, the proposed method can perfectly demonstrate the topologies of micro-structures, which would mitigate the gap between the concept design and manufacturing phases in terms of geometrical boundaries. Particularly, the optimization of the PUC in case 4 starts from the initialization 2 without holes in Fig. 6(b). Observing from the optimal PUC in case 4, new holes can be created to achieve the topological shape evolutions of the PUC. As given in [50], there exists the nucleating mechanism of holes in PLSM because of the natural extension of the normal velocity field to entire design domain.

Meanwhile, the convergent histories of the objective function, volume fraction and configurations of a PUC in case 1 are displayed synchronously in Fig. 7. It can be found that the objective changes remarkably at initial 10 steps because the violation of the volume fraction constraint, and then it starts to increase stably when the constraint function keeps constant. It takes another 140 steps to arrive at the

Table 6
Optimal results for PUCs with maximum bulk modulus.

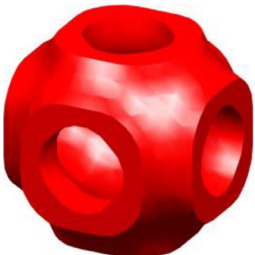
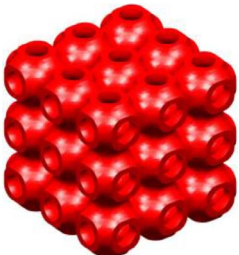
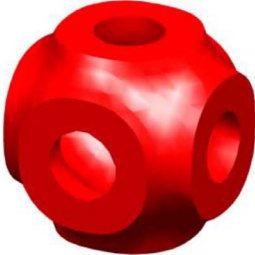
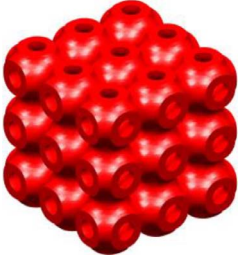
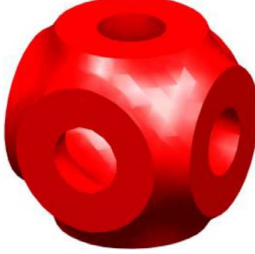
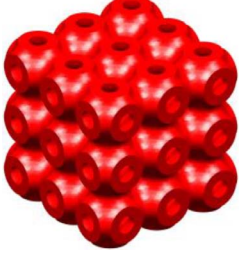
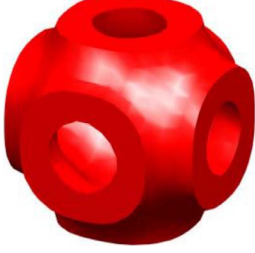
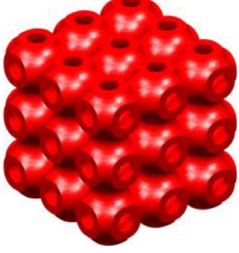




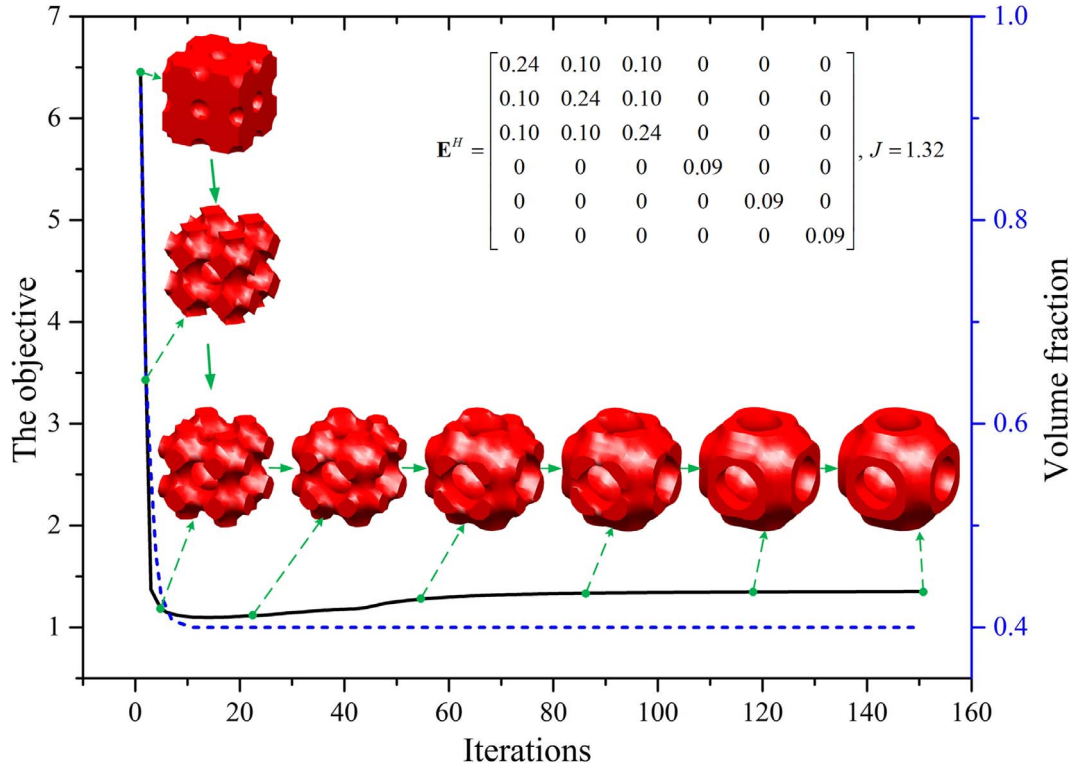
Case	Optimal design of a PUC	3 × 3 × 3 repetitive PUCs	E^H	J
1			$\begin{bmatrix} 0.24 & 0.10 & 0.10 & 0 & 0 & 0 \\ 0.10 & 0.24 & 0.10 & 0 & 0 & 0 \\ 0.10 & 0.10 & 0.24 & 0 & 0 & 0 \\ 0 & 0 & 0 & 0.09 & 0 & 0 \\ 0 & 0 & 0 & 0 & 0.09 & 0 \\ 0 & 0 & 0 & 0 & 0 & 0.09 \end{bmatrix}$	1.32
2			$\begin{bmatrix} 0.29 & 0.12 & 0.12 & 0 & 0 & 0 \\ 0.12 & 0.29 & 0.12 & 0 & 0 & 0 \\ 0.12 & 0.12 & 0.29 & 0 & 0 & 0 \\ 0 & 0 & 0 & 0.11 & 0 & 0 \\ 0 & 0 & 0 & 0 & 0.11 & 0 \\ 0 & 0 & 0 & 0 & 0 & 0.11 \end{bmatrix}$	1.59
3			$\begin{bmatrix} 0.34 & 0.14 & 0.14 & 0 & 0 & 0 \\ 0.14 & 0.34 & 0.14 & 0 & 0 & 0 \\ 0.14 & 0.14 & 0.34 & 0 & 0 & 0 \\ 0 & 0 & 0 & 0.12 & 0 & 0 \\ 0 & 0 & 0 & 0 & 0.12 & 0 \\ 0 & 0 & 0 & 0 & 0 & 0.12 \end{bmatrix}$	1.86
4			$\begin{bmatrix} 0.24 & 0.10 & 0.10 & 0 & 0 & 0 \\ 0.10 & 0.24 & 0.10 & 0 & 0 & 0 \\ 0.10 & 0.10 & 0.24 & 0 & 0 & 0 \\ 0 & 0 & 0 & 0.09 & 0 & 0 \\ 0 & 0 & 0 & 0 & 0.09 & 0 \\ 0 & 0 & 0 & 0 & 0 & 0.09 \end{bmatrix}$	1.32

Table 7

Cross-sectional views of the optimized micro-structured topologies.

Case	1	2	3	4
Cross-sectional views				

**Fig. 7.** Convergent histories of the objective, volume fraction and configuration of a PUC in case 1.

optimal solution. Both of the objective and volume fraction curves have a smooth, fast and stable convergence, which illustrates the high optimization efficiency of the proposed method. This mainly results from that the PLSM mitigates some unfavorable numerical schemes of the LSM in terms of directly solving the H-J PDEs. Moreover, the 3D EBHM can avoid the complex theoretical derivations and numerical implementations of the asymptotic theory. Thus, the proposed method integrating the 3D EBHM with the PLSM can effectively serve for the design of 3D material microstructures.

Additionally, as shown in the third and fourth columns of Table 6, the bulk modulus is increased with the increment of the prescribed volume fraction. It is reasonable that the base material can enhance the stiffness performance of a structure.

6.3. 3D micro-structured materials with maximum shear modulus

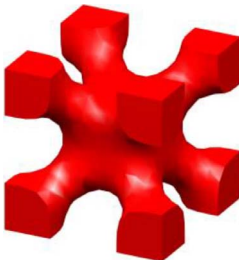
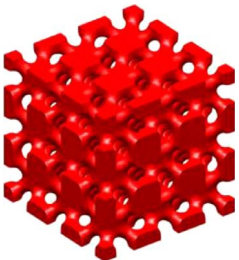

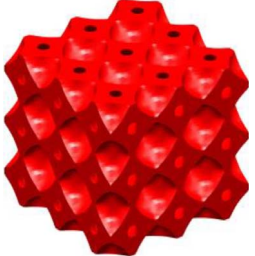

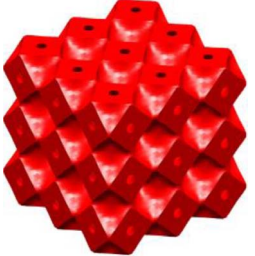
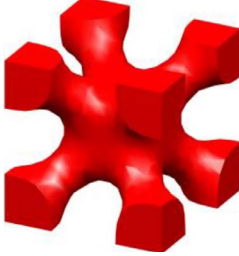
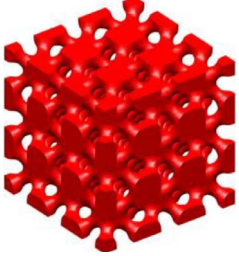
In this section, the proposed method is applied to maximize the shear modulus of PUCs. The corresponding objective function is written as:

$$J(\mathbf{u}, \Phi) = \sum_{i,k=1}^3 E_{ijkl}^H (i \neq j \& k \neq l) \quad (34)$$

The four cases under different initializations and volume fraction constraints in this section are kept the same as the previous maximal bulk modulus example. In Table 8, the optimized topologies of PUCs, $3 \times 3 \times 3$ repetitive PUCs, the homogenized elastic tensor \mathbf{E}^H and the objective J in four cases are presented. These numerical results further demonstrate the feasibility of the proposed method, as well as the 3D EBHM. Similarly, all the optimized topologies of PUCs with maximum shear modulus are featured with smooth boundaries and clear interfaces, shown in the second and third columns of Table 8. The cross-sectional views of configurations of the optimized PUCs in Table 9 can also display the positive characteristic. Hence, the proposed method can perfectly illustrate geometrical configurations of PUCs by the implicit boundary representation model in the PLSM. Additionally, new holes can be created in PUCs under case 4 with the initialization 2 without holes in Fig. 6(b).

Under case 1, the convergent histories of the objective function, volume fraction and topologies of a PUC are displayed in Fig. 8. It can

Table 8
Optimal results for PUCs with maximum shear modulus.



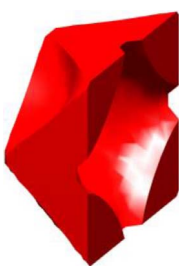

Case	Optimal design of a PUC	$3 \times 3 \times 3$ repetitive PUCs	E^H	J
1			$\begin{bmatrix} 0.20 & 0.07 & 0.07 & 0 & 0 & 0 \\ 0.07 & 0.20 & 0.07 & 0 & 0 & 0 \\ 0.07 & 0.07 & 0.20 & 0 & 0 & 0 \\ 0 & 0 & 0 & 0.11 & 0 & 0 \\ 0 & 0 & 0 & 0 & 0.11 & 0 \\ 0 & 0 & 0 & 0 & 0 & 0.11 \end{bmatrix}$	0.33
2			$\begin{bmatrix} 0.26 & 0.85 & 0.85 & 0 & 0 & 0 \\ 0.85 & 0.26 & 0.85 & 0 & 0 & 0 \\ 0.85 & 0.85 & 0.26 & 0 & 0 & 0 \\ 0 & 0 & 0 & 0.14 & 0 & 0 \\ 0 & 0 & 0 & 0 & 0.14 & 0 \\ 0 & 0 & 0 & 0 & 0 & 0.14 \end{bmatrix}$	0.42
3			$\begin{bmatrix} 0.32 & 0.10 & 0.10 & 0 & 0 & 0 \\ 0.10 & 0.32 & 0.10 & 0 & 0 & 0 \\ 0.10 & 0.10 & 0.32 & 0 & 0 & 0 \\ 0 & 0 & 0 & 0.16 & 0 & 0 \\ 0 & 0 & 0 & 0 & 0.16 & 0 \\ 0 & 0 & 0 & 0 & 0 & 0.16 \end{bmatrix}$	0.48
4			$\begin{bmatrix} 0.20 & 0.07 & 0.07 & 0 & 0 & 0 \\ 0.07 & 0.20 & 0.07 & 0 & 0 & 0 \\ 0.07 & 0.07 & 0.20 & 0 & 0 & 0 \\ 0 & 0 & 0 & 0.11 & 0 & 0 \\ 0 & 0 & 0 & 0 & 0.11 & 0 \\ 0 & 0 & 0 & 0 & 0 & 0.11 \end{bmatrix}$	0.33

be easily seen that the trajectories of the convergent processes show that the objective and volume fraction converge to the optimal solutions rapidly within 20 steps and become plateau afterwards, which shows the high optimization efficiency of the proposed method. Similar to the bulk modulus, the shear modulus increases as the increment of the volume fraction. Hence, in terms of the illustration of geometrical features and optimization efficiency, it would be further indicated that

the proposed method can effectively serve for design of 3D micro-structured materials by sufficiently making use of their individual positive features of both the 3D EBHM and the PLSM.

In conclusion, the systematic design of 3D micro-structured materials is illustrated in Fig. 9. In the first evaluation stage, the 3D EBHM is developed and applied to evaluate macroscopic material effective properties based on the configurations of PUCs. Then, a bridge between

Table 9
Cross-sectional views of the optimized micro-structured topologies.

Case	1	2	3	4
Cross-sectional views				

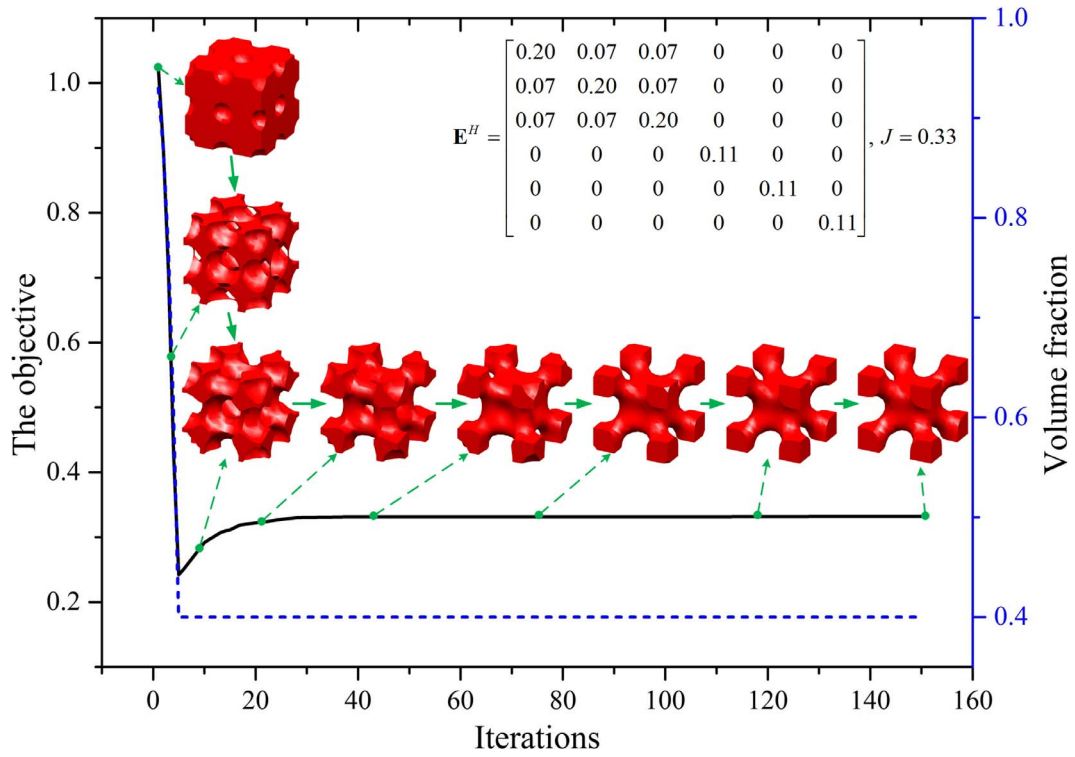


Fig. 8. Convergent histories of the objective, volume fraction and configuration in case 1.

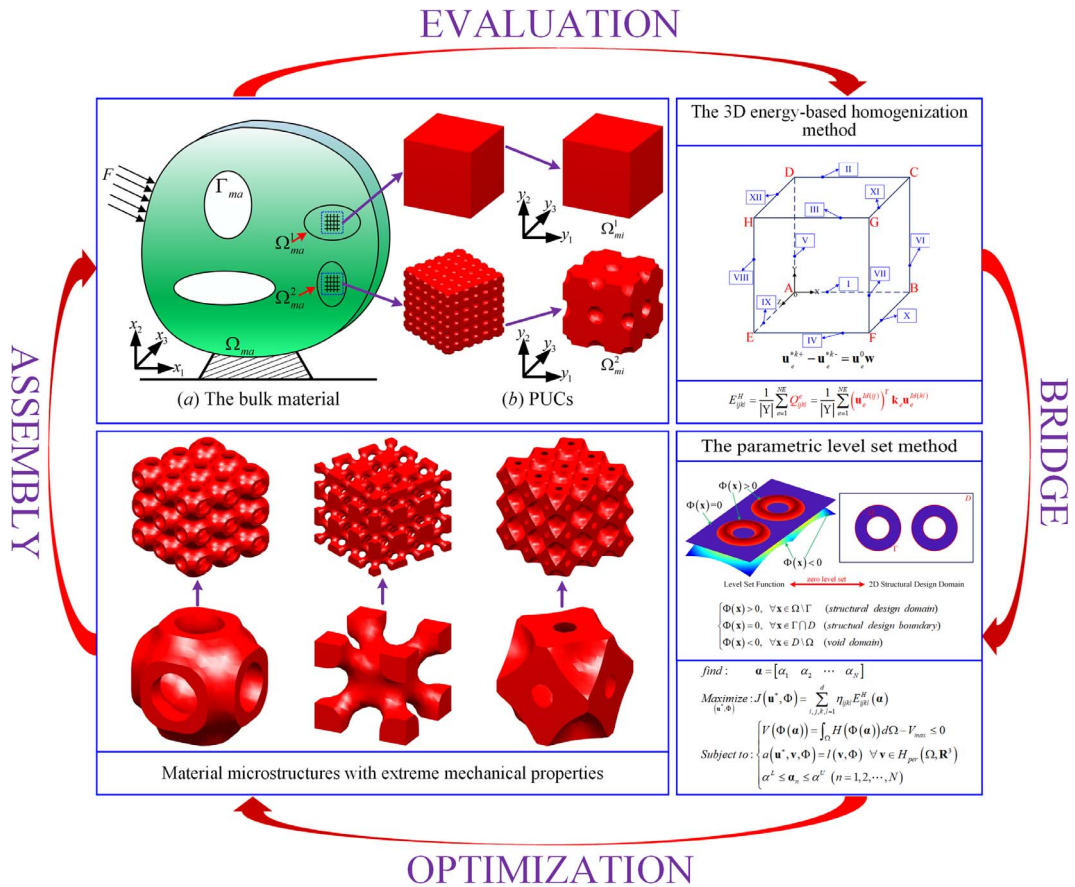


Fig. 9. An illustration of the systematic design of 3D micro-structured materials.

the evaluation and optimization stages is built, where the evaluated effective properties work as the objective. The PLSM is applied to evolve configurations of PUCs until the extreme properties are gained. Finally, the optimized PUCs are periodically arranged in the bulk material during the assembly stage, and the bulk material with extreme properties is obtained.

7. Conclusions and future work

In this study, an effective design method is proposed for the 3D micro-structured materials. It is composed of two aspects: the evaluation and optimization. The evaluation aims at efficiently predicting material effective properties by the 3D EBHM, where the 3D periodic boundary formulation is developed considering three key factors: 3D periodic boundary conditions, 3D boundary constraint equations and the reduced linearly elastic equilibrium equation. The optimization accounts for evolving the configurations of PUCs by the PLSM. Numerical examples can present the positive characteristics of the proposed method. Results show that the proposed method can effectively serve for the design of 3D micro-structured materials by sufficiently making use of the individual positive features of the 3D EBHM and the PLSM.

It should be noted that the developed 3D EBHM is only considered for linearly elastic structures. As part of future work, the 3D EBHM will be extended to evaluate the non-linearly elastic properties. Additionally, design of 3D micro-structured materials with other physical properties can be conducted, like materials with maximum thermal conductivity and thermal expansion coefficient.

Acknowledgments

This work was supported by the National Basic Scientific Research Program of China [grant number JCKY2016110C012] and the National Natural Science Foundation of China [grant numbers 51675196 and 51721092], the Graduates' Innovation Fund of Huazhong University of Science and Technology [grant number 2017YGCXY026], and the China Postdoctoral Science Foundation [grant number 2017M612446].

Supplementary materials

Supplementary material associated with this article can be found, in the online version, at [doi:10.1016/j.advengsoft.2017.12.002](https://doi.org/10.1016/j.advengsoft.2017.12.002).

References

- [1] Gibson LJ, Ashby MF. Cellular solids: structure and properties. Cambridge University Press; 1999.
- [2] Ashby MF, Evans A, Fleck NA, Gibson LJ, Hutchinson JW, Wadley HNG. Metal foams: a design guide. Butterworth-Heinemann; 2000.
- [3] Fleck NA, Ashby MF. Micro-architected materials: past, present and future. *Proc R Soc A* 2010;466(2121):2495–516.
- [4] Cherkav AV, Kohn R. Topics in the mathematical modelling of composite materials. New-York: Springer; 2012.
- [5] Torquato S. Random heterogeneous materials. New-York: Springer; 2002.
- [6] Christensen RM. Mechanics of cellular and other low-density materials. *Int J Solids Struct* 2000;37(1):93–104.
- [7] Osanov M, Guest JK. Topology optimization for architected materials design. *Ann Rev Mater Res* 2016;46:211–33.
- [8] van Dijk NP, Maute K, Langelaar M, Van Keulen F. Level-set methods for structural topology optimization: a review. *Struct Multidiscip Optim* 2013;48(3):437–72.
- [9] Sigmund O, Maute K. Topology optimization approaches. *Struct Multidiscip Optim* 2013;48(6):1031–55.
- [10] Cadman JE, Zhou S, Chen Y, Li Q. On design of multi-functional microstructural materials. *J Mater Sci* 2013;48(1):51–66.
- [11] Bendsoe MP, Kikuchi N. Generating optimal topologies in structural design using a homogenization method. *Comput Methods Appl Mech Eng* 1988;71(2):197–224.
- [12] Zhou M, Rozvany G. The COC algorithm, Part II: Topological, geometrical and generalized shape optimization. *Comput Methods Appl Mech Eng* 1991;89(1–3):309–36.
- [13] Bendsoe MP, Sigmund O. Material interpolation schemes in topology optimization. *Arch Appl Mech* 1999;69:635–54.
- [14] Xie YM, Steven GP. A simple evolutionary procedure for structural optimization. *Comput Struct* 1993;49(5):885–96.
- [15] Sethian JA, Wiegmann A. Structural boundary design via level set and immersed interface methods. *J Comput Phys* 2000;163(2):489–528.
- [16] Wang MY, Wang X, Guo D. A level set method for structural topology optimization. *Comput Methods Appl Mech Eng* 2003;192(1):227–46.
- [17] Allaire G, Jouve F, Toader A-M. Structural optimization using sensitivity analysis and a level-set method. *J Comput Phys* 2004;194(1):363–93.
- [18] Guedes J, Kikuchi N. Preprocessing and postprocessing for materials based on the homogenization method with adaptive finite element methods. *Comput Methods Appl Mech Eng* 1990;83(2):143–98.
- [19] Sigmund O. Materials with prescribed constitutive parameters: an inverse homogenization problem. *Int J Solids Struct* 1994;31(17):2313–29.
- [20] Gibiansky LV, Sigmund O. Multiphase composites with extremal bulk modulus. *J Mech Phys Solids* 2000;48(3):461–98.
- [21] Radman A, Huang X, Xie Y. Topological optimization for the design of microstructures of isotropic cellular materials. *Eng Optim* 2013;45(11):1331–48.
- [22] Andreassen E, Lazarov BS, Sigmund O. Design of manufacturable 3D extremal elastic microstructure. *Mech Mater* 2014;69(1):1–10.
- [23] Long K, Du X, Xu S, Xie YM. Maximizing the effective Young's modulus of a composite material by exploiting the Poisson effect. *Compos Struct* 2016;153:593–600.
- [24] Challis VJ, Guest JK, Grotowski JF, Roberts AP. Computationally generated cross-property bounds for stiffness and fluid permeability using topology optimization. *Int J Solids Struct* 2012;49(23):3397–408.
- [25] Guest JK, Prévost JH. Optimizing multifunctional materials: design of microstructures for maximized stiffness and fluid permeability. *Int J Solids Struct* 2006;43(22):7028–47.
- [26] Wang Y, Gao J, Luo Z, Brown T, Zhang N. Level-set topology optimization for multimaterial and multifunctional mechanical metamaterials. *Eng Optim* 2017;49(1):22–42.
- [27] Clausen A, Wang F, Jensen JS, Sigmund O, Lewis JA. Topology optimized architectures with programmable Poisson's ratio over large deformations. *Adv Mater* 2015;27(37):5523–7.
- [28] Xia L, Breitkopf P. Design of materials using topology optimization and energy-based homogenization approach in Matlab. *Struct Multidiscip Optim* 2015;52(6):1229–41.
- [29] Wang Y, Luo Z, Zhang N, Kang Z. Topological shape optimization of microstructural metamaterials using a level set method. *Comput Mater Sci* 2014;87:178–86.
- [30] Da D, Chen J, Cui X, Li G. Design of materials using hybrid cellular automata. *Struct Multidiscip Optim* 2017;56(1):131–7.
- [31] Sigmund O, Torquato S. Design of materials with extreme thermal expansion using a three-phase topology optimization method. *J Mech Phys Solids* 1997;45(6):1037–67.
- [32] Berger J, Wadley H, McMeeking R. Mechanical metamaterials at the theoretical limit of isotropic elastic stiffness. *Nature* 2017;543(7646):533–7.
- [33] Hassani B, Hinton E. A review of homogenization and topology optimization I-homogenization theory for media with periodic structure. *Comput Struct* 1998;69(6):707–17.
- [34] Hassani B, Hinton E. A review of homogenization and topology optimization II-analytical and numerical solution of homogenization equations. *Comput Struct* 1998;69(6):719–38.
- [35] Andreassen E, Andreassen CS. How to determine composite material properties using numerical homogenization. *Comput Mater Sci* 2014;83(2):488–95.
- [36] Du Y, Li H, Luo Z, Tian Q. Topological design optimization of lattice structures to maximize shear stiffness. *Adv Eng Softw* 2017;112:211–21.
- [37] Zhang WH, Dai GM, Wang FW, Sun SP, Bassir H. Using strain energy-based prediction of effective elastic properties in topology optimization of material microstructures. *Acta Mech Sin* 2007;23(1):77–89.
- [38] Xia L, Xia Q, Huang X, Xie YM. Bi-directional evolutionary structural optimization on advanced structures and materials: a comprehensive review. *Arch Comput Method Eng* 2016. <http://dx.doi.org/10.1007/s11831-016-9170-7>.
- [39] Allaire G, Jouve F. A level-set method for vibration and multiple loads structural optimization. *Comput Methods Appl Mech Eng* 2005;194(30):3269–90.
- [40] Yamada T, Izui K, Nishiwaki S. A level set-based topology optimization method for maximizing thermal diffusivity in problems including design-dependent effects. *J Mech Des* 2011;133. 031011-1-9.
- [41] Wang Y, Wang MY, Chen F. Structure-material integrated design by level sets. *Struct Multidiscip Optim* 2016;54(5):1145–56.
- [42] Zhou S, Li W, Sun G, Li Q. A level-set procedure for the design of electromagnetic metamaterials. *Opt Express* 2010;18(1):6693–702.
- [43] Otomori M, Yamada T, Izui K, Nishiwaki S, Andkjær J. A topology optimization method based on the level set method for the design of negative permeability dielectric metamaterials. *Comput Methods Appl Mech Eng* 2012;237:192–211.
- [44] Guo X, Zhang WS, Zhong WL. Doing topology optimization explicitly and geometrically—a new moving morphable components based framework. *J Appl Mech* 2014. 81 081009:1-12.
- [45] Wang S, Wang MY. Radial basis functions and level set method for structural topology optimization. *Int J Numer Meth Eng* 2006;65(12):2060–90.
- [46] Xia Q, Wang MY, Wang S, Chen S. Semi-Lagrange method for level-set-based structural topology and shape optimization. *Struct Multidiscip Optim* 2006;31(6):419–29.
- [47] Yamada T, Izui K, Nishiwaki S, Takezawa A. A topology optimization method based on the level set method incorporating a fictitious interface energy. *Comput Methods Appl Mech Eng* 2010;199(45):2876–91.
- [48] Yamasaki S, Nishiwaki S, Yamada T, Izui K, Yoshimura M. A structural optimization method based on the level set method using a new geometry-based re-initialization scheme. *Int J Numer Meth Eng* 2010;83(12):1580–624.

- [49] Luo Z, Wang MY, Wang S, Wei P. A level set-based parameterization method for structural shape and topology optimization. *Int J Numer Meth Eng* 2008;76(1):1–26.
- [50] Luo Z, Tong L, Kang Z. A level set method for structural shape and topology optimization using radial basis functions. *Comput Struct* 2009;87:425–34.
- [51] Svanberg K. The method of moving asymptotes—a new method for structural optimization. *Int J Numer Meth Eng* 1987;24:359–73.
- [52] Chu S, Gao L, Xiao M, Luo Z, Li H. Stress-based multi-material topology optimization of compliant mechanisms. *Int J Numer Meth Eng* 2017<https://doi.org/10.1002/nme.5697>.
- [53] Li H, Li P, Gao L, Zhang L, Wu T. A level set method for topological shape optimization of 3D structures with extrusion constraints. *Comput Methods Appl Mech Eng* 2015;283:615–35.
- [54] Wu J, Gao J, Luo Z, Brown T. Robust topology optimization for structures under interval uncertainty. *Adv Eng Softw* 2016;99:36–48.
- [55] Wang Y, Luo Z, Kang Z, Zhang N. A multi-material level set-based topology and shape optimization method. *Comput Methods Appl Mech Eng* 2015;283:1570–86.
- [56] Li H, Luo Z, Zhang N, Gao L, Brown T. Integrated design of cellular composites using a level-set topology optimization method. *Comput Methods Appl Mech Eng* 2016;309:453–75.
- [57] Michel J-C, Moulinec H, Suquet P. Effective properties of composite materials with periodic microstructure: a computational approach. *Comput Methods Appl Mech Eng* 1999;172:109–43.
- [58] Xia Z, Zhou C, Yong Q, Wang X. On selection of repeated unit cell model and application of unified periodic boundary conditions in micro-mechanical analysis of composites. *Int J Solids Struct* 2006;43(2):266–78.
- [59] Wendland H. Piecewise polynomial, positive definite and compactly supported radial functions of minimal degree. *Adv Comput Math* 1995;4(1):389–96.
- [60] Osher S, Fedkiw R. Level set methods and dynamic implicit surfaces. New-York: Springer; 2006.